Journal of Power Sources 193 (2009) 625–631

Contents lists available at ScienceDirect

Journal of Power Sources

journal homepage: www.elsevier.com/locate/jpowsour

Experimental characterization of glass–ceramic seal properties and their constitutive implementation in solid oxide fuel cell stack models

E.V. Stephens [a], J.S. Vetrano [b], B.J. Koeppel [a], Y. Chou [a], X. Sun [a], M.A. Khaleel [a,*]

[a] Pacific Northwest National Laboratory, PO Box 999, Richland, WA 99352, USA
[b] Office of Basic Energy Science, U.S. Department of Energy, 1000 Independence Avenue SW, Washington, DC 20585-1290, USA

ARTICLE INFO

Article history:
Received 26 January 2009
Received in revised form 24 February 2009
Accepted 24 February 2009
Available online 13 March 2009

Keywords:
Glass–ceramic sealant
Solid oxide fuel cell
Property characterization
Finite element analysis

ABSTRACT

This paper discusses experimental determination of solid oxide fuel cell (SOFC) glass–ceramic seal material properties and seal/interconnect interfacial properties to support development and optimization of SOFC designs through modeling. Material property experiments such as dynamic resonance, dilatometry, flexure, creep, tensile, and shear tests were performed on PNNL's glass–ceramic sealant material, designated as G18, to obtain property data essential to constitutive and numerical model development. Characterization methods for the physical, mechanical, and interfacial properties of the sealing material, results, and their application to the constitutive implementation in SOFC stack modeling are described.

Published by Elsevier B.V.

1. Introduction

Computer modeling of solid oxide fuel cells (SOFCs) allows researchers to more fully understand how design choices will impact the overall system performance. Models provide an efficient method for evaluating new design possibilities and evaluating a variety of conditions in a short period of time. However, models are most useful when they are constructed from accurate input data such as thermal-mechanical properties for the various component materials and interfaces. Experimental tests need to be performed to identify the material coefficients and to validate the developed models.

In this study, material characterization and testing was performed on a PNNL developed barium–calcium–aluminosilicate based glass sealing material [1,2], referred to as G18. Glass–ceramic materials are commonly used to join different components of a planar SOFC system in order to separate the fuel and oxidant flow streams. The amorphous glass material is heated and wets the surfaces to be joined, but then rapidly devitrifies during heat treatment to provide stiffness and strength to the seal. They have been found suitable to bond different SOFC components because of their chemical compatibility with other fuel cell components, low volatility, high electrical resistance, and low coefficient of thermal expansion (CTE) mismatch with joined components. In addition, their excellent hermeticity, low cost, ease of fabrication, and ability to be tailored for improved properties makes it a desirable sealing material.

For SOFC stack design, it is essential to characterize the properties and behaviors of the constituent layers. An understanding of the behavior of materials as a function of time, temperature, and deformation is needed for developing property predictions and numerical models of the system. G18 is susceptible to damage and cracking caused by operational thermal stresses as well as cyclic thermal loading in the stack [3]. Experimental observations have indicated that even a few thermal cycles can cause strength reduction [4] and cracking of the seals, which leads to reduced performance and loss of cell integrity. In addition, a sealing assembly may have multiple interfacial layers including an oxide scale layer, coatings applied for corrosion protection, and reaction zones with formation of phases, depletion of elements, or void generation [5]. Characterization of the seal interfacial layers must also be addressed since they can potentially be degraded due to chemical reactions and affect the structural integrity of the stack.

This paper first describes the experimental procedures in characterizing the bulk G18 properties and the interfacial strength properties between the seal material and interconnect component. In this work, experimental testing was conducted based on various ASTM standards [6–10] to determine the relevant temperature-dependent physical, mechanical, and interfacial properties. These properties include temperature-dependent elastic modulus, thermal expansion, bulk strength, and interfacial strength as well as temperature and loading rate-dependent creep behaviors. Next, the typical property measurements are presented and discussed. Finally, we present the procedures for implementing these results

* Corresponding author.
E-mail address: moe.khaleel@pnl.gov (M.A. Khaleel).

0378-7753/$ – see front matter. Published by Elsevier B.V.
doi:10.1016/j.jpowsour.2009.02.080

in different constitutive models in order to capture the short-term, long-term and time-dependent behaviors of the glass–ceramic seal in stack performance simulations.

2. Seal specimen preparation

The G18 material specimens utilized in this study were produced either through tape casting or as a paste from the powder form. All specimens for bulk glass property characterization were cut and machined from fired thick plates, which were produced by conventional tape casting of G18 glass powders in an organic solvent system and dried in ambient air before lamination with a hot press at approximately 70–80 °C. The laminated multiple G18 tapes were fired to burn away all the organics at 500–600 °C for 2 h followed by an 850 °C heat treatment for 1 h and then a final 750 °C heat treatment for either 4 h or 1000 h (1000 h is also referred to as the "aged" condition). After heat treatment, the G18 glass blocks were ground flat and cut into specimens. Parallelepiped specimens with a nominal 50.75 mm × 25.34 mm × 5.96 mm geometry were used for the elastic property measurements. Flexural bend bar specimens with a nominal depth, width, and length of 3 mm × 4 mm × 45 mm were used for the coefficient of thermal expansion and flexural strength measurements. The edges of the bend bars on the tensile side were rounded with SiC #800 grit paper to remove any stress concentrations from machining defects. Additional cylindrical specimens with a nominal 5 mm diameter and a 10 mm height were also machined from the G18 blocks for use in the relaxation and creep tests.

All specimens for interfacial property characterization were produced in a paste form of the G18 material and dispensed using an automated, air-pressurized syringe setup onto bare, 0.5 mm-thick, Crofer 22 APU washers brazed onto sample holders. This replicates the seal and interconnect material interface. The paste was dried in air and two halves of the samples were placed face to face, loaded at 38 kPa and heat treated in a furnace at 850 °C for 1 h and then heat treated at 750 °C for 4 h. A 10 mm diameter washer was utilized for the tensile specimen holders and a washer with a 12.7 mm inner radius and 16.7 mm outer radius was used for the torsion specimen holders. The amount of material and compressive loading was adjusted so that there was a minimal amount of overflow as it softened during the initial heat treatment and resulted in a final thickness of approximately 500 μm.

3. Experimental characterization procedures

3.1. Bulk glass property measurements

3.1.1. Elastic modulus

Dynamic resonance tests were performed to determine the elastic properties of the G18 material at ambient and elevated temperatures. The Young's and shear moduli were measured following ASTM Standard C1198-01 [6]. Resonant frequencies were measured at room temperature and in 100 °C intervals from 200 to 600 °C for the 4 h heat-treated specimen, and measured at room temperature and in 100 °C intervals from 200 to 800 °C for the 1000 h heat-treated, aged specimen. At the end of each test, an additional measurement was repeated near ambient temperature. The furnace was heated at a rate of approximately 12 °C min^{-1}, and was held for 15 min at each temperature for equilibration. The Young's and shear moduli were then used to calculate Poisson's ratio, $\nu = (E/2G) - 1$, where E is the elastic modulus and G is the shear modulus.

3.1.2. Coefficient of thermal expansion (CTE)

The coefficient of thermal expansion of the G18 was measured using dilatometry according to ASTM Standard E228-95 [7]. A Unitherm Model 1161 dilatometer system with a heating and cooling rate of 2 °C min^{-1} from room temperature to 1000 °C was utilized. For both the 4 h and 1000 h heat-treated specimens, the linear thermal expansion test was conducted for three heating and cooling cycles in air. The third thermal cycle was used to define the average CTE using the lowest common reference temperature during the test, T_{ref} = 88.8 °C. The average CTE α_{avg} as a function of temperature T was based on the specimen expansion difference ΔL from the length L_{ref} at the reference temperature T_{ref} according to the following relation:

$$\frac{\Delta L}{L_{ref}} = \alpha_{avg}(T - T_{ref}) \quad (1)$$

3.1.3. Bulk strength

Four-point flexure bend tests were conducted utilizing ASTM Standard C1161-02 [8] and C1211-02 [9] to characterize the bulk strength of the G18 material at different temperatures ranging from room temperature to 800 °C. Tests were conducted at room temperature, 700, 750, and 800 °C. Specimens were tested in an Instron mechanical test frame (Model 5581) using a fully articulated SiC test fixture with an inner span of 20 mm and outer span of 40 mm. The cross-head speed was set at 0.5 mm min^{-1}. For testing at elevated temperatures, the sample was heated in a clam shell high temperature furnace with a heating rate of 10 °C min^{-1} to the test temperature and held for 30–45 min before the bend test. All bend tests were conducted in air without environment control. For each temperature, a minimum of eight bend bars were tested. A load versus deflection curve without any specimen presence was also obtained at 800 °C to assess load train compliance.

Additional bend bar tests were performed at multiple loading rates to observe deformation response for the 4 h heat-treated specimens. For these tests, a different batch of specimens was processed. The bend bar tests were performed at various cross-head speeds of 0.025–0.5 mm min^{-1} resulting in strain rates of approximately 5e^{-6} to 1e^{-5} s^{-1}. All calculations for stress–strain curves were based on elastic beam flexure equations.

3.1.4. Time and temperature-dependent creep properties

Stress relaxation tests and short-term compression creep tests were performed on the 4 h heat-treated specimens at various elevated test temperatures (700, 750 and 800 °C). For the stress relaxation tests, the specimen was compressed to a nominal strain of 0.5% at each test temperature, the cross-head displacement was then locked, and the load cell reading was used to calculate stress relaxation. For the creep compression tests, three specimens at each temperature were loaded at varying load levels ranging from an applied stress of 17–50 MPa at 700 °C, 14–37 MPa at 750 °C, and 10–30 MPa at 800 °C to measure the creep strain response with time. Mechanical testing was performed on a MTS servo-hydraulic test frame with a vertical clamshell-type furnace. Pull rods were machined from Invar to reduce thermal expansion effects, and the exposed portions of the measurement system were thermally shielded. An Inconel "cage" was utilized to convert the tensile motion of the test frame into compressive loading for the test specimen. This consists essentially of a tube within a tube, both with side cutouts for visualization, and integral platens to compress the sample.

3.2. Interfacial property measurements

Tensile and torsion interfacial strength tests were performed to characterize the interfacial quality between the 4 h heat-treated G18 and the interconnect material substrate, Crofer 22 APU. The tension tests were based on ASTM D2095 [10] developed for measuring tensile strength of adhesives. Care was taken to properly align the

samples and the pull rod assembly to ensure only tensile forces was applied and bending moments were minimized. The average interfacial strength was calculated using $\sigma = P/A$ where P is the applied tensile load and A is the specimen area.

Torsion tests were performed to characterize the interfacial shear strength between the G18 glass seal material and Crofer 22. The torsion tests to measure the shear strength was based on ASTM F734-95 [11], a standard developed to test bonding strength of fusion bonded aerospace glazes. The specimen configuration consists of a tubular cross-section, and the maximum shear strength, τ_{max}, was calculated as the following:

$$\tau_{max} = \frac{Tr_o}{J} \quad (2)$$

$$J = \frac{\pi}{2}(r_o^4 - r_i^4) \quad (3)$$

where T is the torque, J is the polar moment of inertia, r_o is the outer radius, and r_i is the inner radius. A stepper motor was utilized to apply torque at a rate of $0.02^\circ\ s^{-1}$. The specimens were held in a horizontal clam shell furnace and tests were performed at 25, 700, 750, and 800 °C.

4. Results and discussion

4.1. Bulk glass seal properties

4.1.1. Elastic modulus

Tables 1 and 2 list the elastic properties of the G18 glass–ceramic sealant material measured by dynamic resonance. For 4 h heat-treated G18, both the Young's modulus and shear modulus decrease with increasing test temperature. This is consistent with the expected behavior of materials at high temperature but may have been further influenced by the softening of the glass phase present in these specimens. Additional room temperature measurements taken again after the high temperature tests achieve the same moduli as the pre-test values.

Table 1
G18 elastic property results for 4 h heat-treated specimen at room and elevated temperatures. A second room temperature measurement was performed after the elevated test temperature measurements.

Test temperature (C)	Elastic modulus (GPa)	Shear modulus (GPa)	Poisson's ratio
22	77.7 ± 0.4	30.5 ± 0.1	0.270 ± 0.002
200	75.8 ± 0.4	29.7 ± 0.1	0.270 ± 0.002
300	74.3 ± 0.4	29.2 ± 0.1	0.270 ± 0.002
400	71.7 ± 0.3	28.0 ± 0.1	0.280 ± 0.002
500	70.6 ± 0.3	27.6 ± 0.1	0.280 ± 0.002
600	67.7 ± 0.3	26.4 ± 0.1	0.280 ± 0.002
30	78.1 ± 0.4	30.6 ± 0.1	0.280 ± 0.002

Table 2
G18 elastic property results for 1000 h heat-treated specimen at room and elevated temperatures. A second room temperature measurement was performed after the elevated test temperature measurements.

Test temperature (C)	Elastic modulus (GPa)	Shear modulus (GPa)	Poisson's ratio
22	60.8 ± 0.3	25.7 ± 0.1	0.183 ± 0.001
200	61.0 ± 0.3	25.9 ± 0.1	0.179 ± 0.001
300	62.2 ± 0.3	26.0 ± 0.1	0.196 ± 0.001
400	69.7 ± 0.3	27.8 ± 0.1	0.256 ± 0.002
500	70.2 ± 0.3	27.8 ± 0.1	0.261 ± 0.002
600	70.3 ± 0.3	27.7 ± 0.1	0.268 ± 0.002
700	69.2 ± 0.3	27.3 ± 0.1	0.266 ± 0.002
800	67.4 ± 0.3	26.5 ± 0.1	0.272 ± 0.002
30	53.2 ± 0.3	23.3 ± 0.1	0.143 ± 0.001

Table 3
G18 coefficient of thermal expansion results for 4 h and 1000 h heat-treated specimen.

Temperature (°C)	Average CTE 4 h heat-treated ($1e^6$/°C)	Average CTE 1000 h heat-treated ($1e^6$/°C)
0	10.5	10.9
200	10.5	10.9
250	10.8	
300	10.9	
370	11.8	
400		10.9
480	11.8	
560	12.0	
600		11.1
610	13.2	
650	13.7	
700	13.5	
800	13.0	11.1
850	12.8	
1000	12.8	11.1

The measured Young's modulus and shear modulus for the 1000 h heat-treated G18 show some very distinct and interesting features. For temperatures lower than 400 °C, both Young's modulus and shear modulus increase with increasing test temperature. The moduli exhibit somewhat temperature independent behaviors from 400 to 600 °C. Above 600 °C, the moduli start to decrease with increasing temperature.

For temperatures lower than 400 °C, the measured modulus for the aged glass–ceramic sealant is consistently less than that of the 4-h treat-treated samples. At about 500 °C, the moduli for the aged and non-aged samples cross over. For temperatures above 600 °C, the moduli trend reverses itself: the modulus for 1000 h heat-treated G18 is higher than that of the 4 h heat-treated G18. The details on the effects of aging, cooling-induced micro-voids and possible reheating related self-healing have been discussed by Liu et al. [12]. It is believed that some microstructure level damage may have occurred during the aging process and that the specimen exhibits some degree of self-healing behaviors because of the flow characteristics of the glass phase at temperature above 400 °C.

4.1.2. Coefficient of thermal expansion (CTE)

Table 3 lists the measured coefficient of thermal expansion for the 4 and 1000 h heat-treated G18 specimens. The 4 h heat-treated samples show an increasing CTE with increasing temperature up to 650 °C. Above 650 °C, a very slight CTE drop is observed with temperature increase up to 1000 °C. In contrast, almost temperature independent CTE results are obtained for the aged, 1000 h heat-treated specimen. These results suggest a less influence of the glassy phase in the aged G18 material which is brought by the dominance of the higher volume fraction of crystalline phase in the aged G18.

4.1.3. Bulk strength

Flexural bending tests for the G18 glass–ceramic sealing material were completed at test temperatures of 25, 700, 750, and 800 °C. The load versus displacement curves for the cross-head were obtained. Fig. 1 illustrates the mean strength versus temperature results for the 4 h heat-treated and 1000 h heat-treated specimens. For all the cases tested, the bulk G18 strength decreased as the temperature increased.

Fig. 2 shows the typical stress–strain response of the flexural specimens for each heat treatment and temperature condition. The overall stress–strain response was apparently linear for each material at test temperatures up to 700 °C, but then the materials exhibited a nonlinear response at test temperatures greater than 700 °C, which is induced by the creep behavior of the amorphous glass phase at high temperature. In addition to the lower strength, the 1000-h aged specimens also had a consistently lower failure

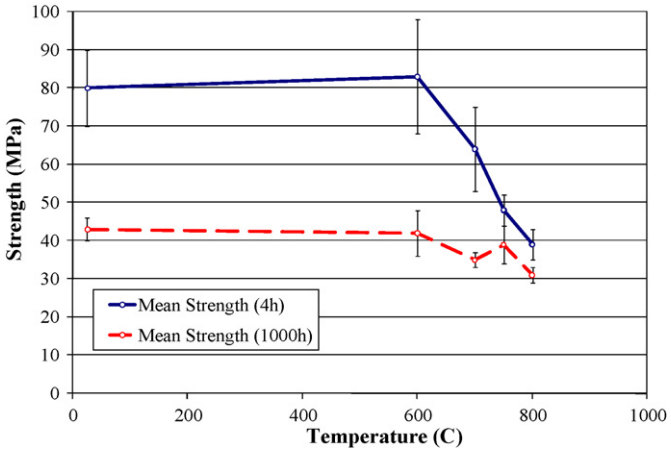

Fig. 1. Dependence of the mean flexural strength results of the 4 and 1000 h heat-treated G18 glass–ceramic specimens with temperature increase.

strain at each respective temperature in comparison to the 4-h un-aged specimens. Higher crystallinity in the 1000 h heat-treated specimens was expected to provide higher strengths. However, as pointed out by Liu et al. [12], shrinkage micro-voids will likely form during cooling process for the aged samples due to the CTE differences between the crystalline and the amorphous phases. Fig. 3(a) and (b) compare the microstructures of the 4-h un-aged and 1000-h aged G18 specimens. The growth and coalescence of these micro-voids and micro-cracks can noticeably degrade the strength and ductility of the glass–ceramic seal at various testing temperatures.

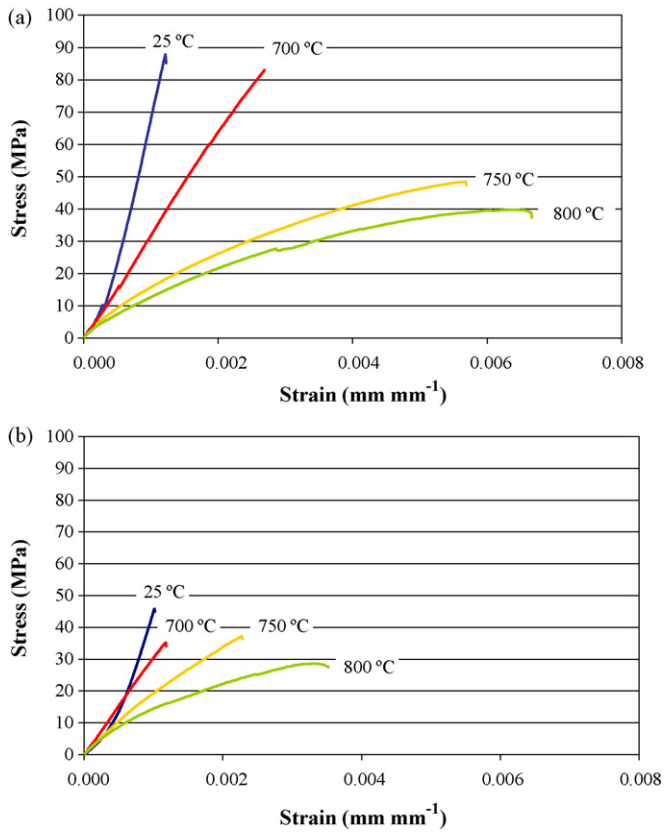

Fig. 2. Stress–strain responses of the 4 h (a) and 1000 h (b) heat-treated G18 glass–ceramic flexural specimens at each test temperature.

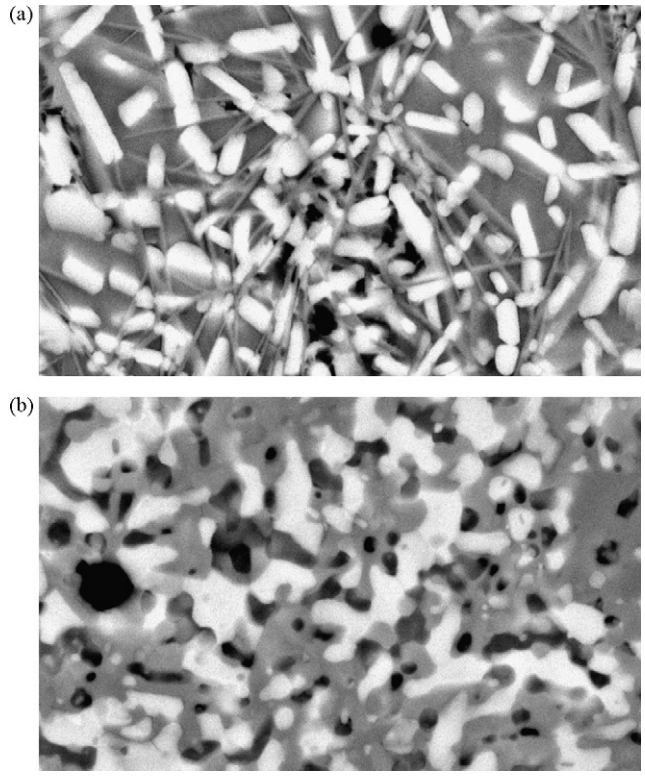

Fig. 3. SEM image (magnification: 5000×) of G18 microstructures after processing and devitrification; (a) 4 h heat-treated, un-aged; (b) 1000 h heat-treated, aged.

4.1.4. Loading rate and temperature-dependent creep properties

The influences of batch-to-batch variation and loading rate on the measured stress versus strain behaviors for flexural tests at 750 °C are shown in Fig. 4. Here, the responses of two batches of G18 with similar 4-h heat treatment schedule are shown to vary significantly. This response variation indicates that the microstructures are different and the crystallization rates can be quite sensitive to the glass precursors and the associated processing procedures. These property variations may be important for consideration in the cell initial assembly during which the seals complete devitrification.

The measured stress–strain responses under different loading rates indicate that viscous softening of the material primarily occurs at lower loading rates due to the residual glass phase in the material. As the loading rate increases, the viscous-flow characteristics of G18

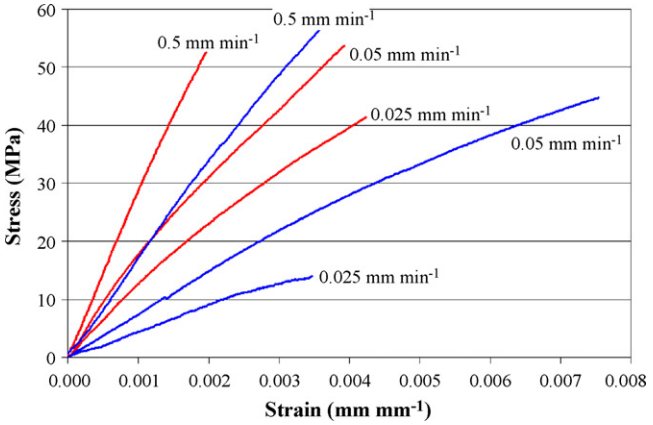

Fig. 4. Stress–strain response of the 4 h heat-treated G18 glass–ceramic flexural specimens as a function of the loading rate. The red and blue lines indicate different specimen batches.

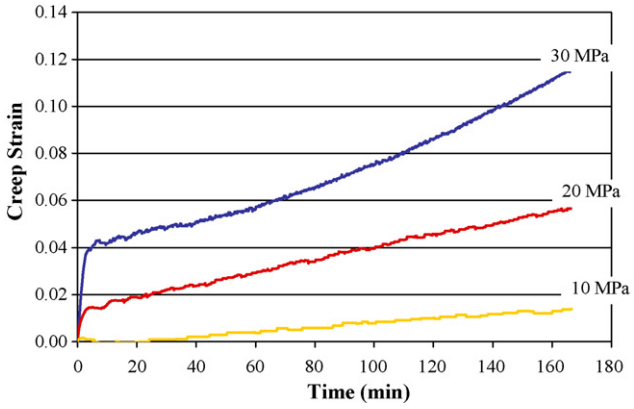

Fig. 5. Short-term creep strain results for the 4h heat-treated G18 glass–ceramic cylinders at 800 °C at three different applied stresses levels.

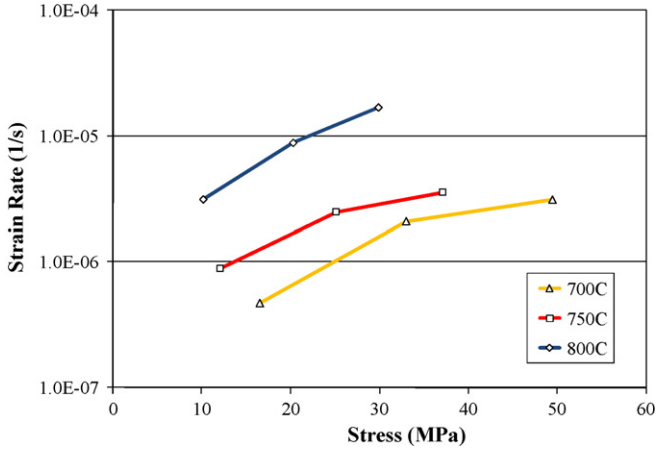

Fig. 6. Creep strain rate results for the 4 h heat-treated G18 glass–ceramic cylinders.

decreases, consistent with the rate-dependent behaviors of visco-elastic or visco-plastic materials.

Short-term compression creep tests were also performed to evaluate the creep strain with time for 4 h heat-treated G18 specimen under different applied stress and temperature. For example, Fig. 5 shows some typical creep strain versus time curves for G18 at 800 °C under different applied stresses. Note that the short-term creep strain increase with time is approximately linear after the initial rapid primary creep strain. With increasing applied stress and temperature, G18 experiences higher creep strain rate, see Fig. 6.

4.2. Glass seal interfacial properties

Tables 4 and 5 present the mean interfacial strength data between the G18 glass–ceramic seal material and Crofer 22 APU substrate at temperatures ranging from 25 to 800 °C in both tension and shear. The interfacial strengths in both of these test configurations follow the same decreasing trend with increasing test temperature. At the same testing temperature, the shear strength of the interface is much higher than its tensile strength, similar to the strength characteristics of a typical adhesive bond under different loading mode. Moreover, when compared with the bulk flexural strengths for the 4-h un-aged condition for G18 (Fig. 1), one can see that the interfacial tensile strengths are much lower in this sealing analog configuration. Examination of the fracture surfaces also reveals two different failure modes in the tensile tests: glass bulk failure mode referring to failure occurring through the glass layer, and interfacial failure (IF) mode referring to failure occurring at the glass–Crofer interface. It is consistently observed that an interfacial failure mode generates lower bond strength in comparison to bulk glass failure, see Fig. 7. This is also analogous to the strength difference between adhesive failure and cohesive failure typically observed in adhesive bonds.

Table 4
Interfacial tensile strength properties of G18 and interconnect substrate, Crofer 22 APU. Failures that occurred at the interface are denoted by "IF".

Test temperature (°C)	Failure mode	Mean failure stress (MPa)
25	Glass bulk	24.0
25	IF	18.0
700	Glass bulk	25.0
700	IF	16.5
750	IF	12.2
800	IF	5.3

Table 5
Interfacial shear strength properties of G18 and interconnect substrate, Crofer 22 APU. Failures that occurred at the interface are denoted by "IF".

Test temperature (°C)	Failure mode	Mean max shear stress (MPa)
25	IF	47.1
700	IF	51.6
750	IF	23.5
800	IF	17.6

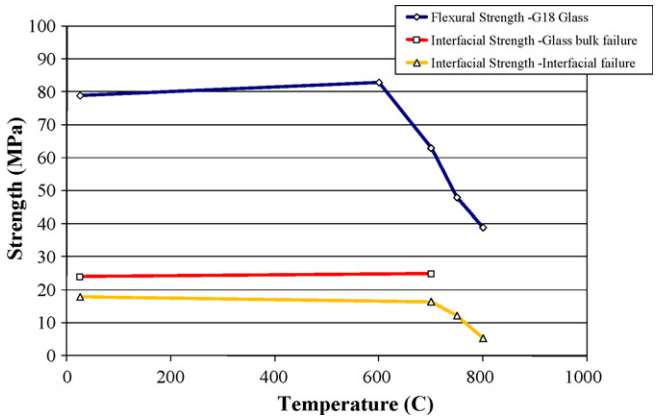

Fig. 7. Strength comparisons of G18 bulk glass and interfacial tensile strengths based on failure mode.

5. Constitutive implementations in stack modeling

5.1. Development of constitutive relations

Obtaining the physical and mechanical properties of the G18 seal material and characterizing the microstructure can aid in the development of constitutive laws governing the glass seal behaviors under different temperatures and loading conditions. These constitutive laws can then be implemented in the stack simulations to accurately predict the time and temperature-dependent seal behaviors. These models in conjunction with parametric stress analyses of SOFC stacks can also be used to identify the preferred range of material properties to avoid seal failure which will help to direct glass–ceramic material development to achieve reliable sealing of stacks. In this section, we will summarize the constitutive implementations of the material properties obtained in the previous sections.

5.1.1. Coefficient of thermal expansion

The coefficient of thermal expansion is probably the most important material property for modeling of the SOFC. The mismatches of CTE between joined components in the stack are the primary source of cell deformations and component stresses, so accurate representation of the CTE is essential. The average CTE for the seal showed a clear variation with temperature for the 4 h heat-treated sealant (Table 3), where the difference between elevated and room temperatures was more than 15%. Therefore the full temperature-dependent values were always used in the models rather than a constant value to evaluate stresses at both the operating and shut-down conditions. Thermal strain computations in the structural stack model also required definition of the temperature at which thermal strain is zero. This value has not been experimentally measured, but based on the heat treatment schedule the zero strain temperature for the G18 sealant was assumed to be within the processing range of 750–850 °C. Depending on the modeling platform used, the average CTE values α_{avg} presented in Table 3 may need to be converted to instantaneous CTE values α_{inst} using the relation

$$\alpha_{inst} = \alpha_{avg} + \frac{d\alpha_{avg}}{dT}(T - T_{sf}) \quad (4)$$

where T is temperature and T_{sf} is the temperature at zero thermal strain.

5.1.2. Elastic modulus

A phenomenological model has been developed to model the temperature-dependent Young's modulus of G18 as presented in Tables 1 and 2 considering the combined effects of aging, micro-voids, and possible self-healing [12]. An aging time-dependent crystalline content model was first developed to describe the increase of the crystalline content due to the continuing devitrification under high operating temperature. A continuum damage mechanics (CDM) model was then adapted to model the effects of both cooling-induced micro-voids and reheating induced self-healing. By considering the combined effects of aging, micro-voids and self-healing, Liu et al. [12] demonstrated that a simple phenomenological model can be used to capture the distinct features of the moduli 'cross over' as discussed in the previous sections.

5.1.3. Bulk strength

This section summarizes the application of a CDM-based constitutive model in simulating the temperature-dependent stress versus strain behavior and the strength of G18 [13]. The model accounts for the material damage due to various mechanisms in a purely phenomenological manner through a scalar damage variable that governs the reduction of the homogenized elastic modulus. The elastic deformation energy was taken as the thermodynamic potential to derive the constitutive relations and the thermodynamic force associated with the damage variable. The damage threshold function was numerically determined using the experimental stress–strain curves obtained in the four-point bending tests. The viscous behavior at high temperatures ($T > 700$ °C), which results from the residual glassy phase, is described by a Kelvin–Voigt-type model accounting for a viscous stress [14]. Details of the constitutive model development and validation can be found in Nguyen et al. [13]. The model was used to simulate the four-point bending tests of G18 under different temperatures, and very good agreements have been obtained with the experimental measurement curves such as the ones shown in Fig. 3. The models were then used to predict the regions of likely sealant failure in multi-cell stacks under thermal cycling loading [3].

5.1.4. Temperature and rate-dependent creep properties

In order to model the temperature and loading rate-dependent nonlinear creep behaviors of G18, a visco-elastic damage model was first developed that can capture the nonlinear material response due to both progressive damage and viscous flow of the residual glass in the glass–ceramic material [15]. A modification of the basic Maxwell model [14] has been made to include the contribution of damage to the nonlinear stress–strain response. Experimental tests such as those in Figs. 4 and 5 were used for identifying the material coefficients and for validating the developed model. The model can well capture the initial stage of relaxation that is characterized by a fast stress reduction. Nevertheless, the Maxwell-type model significantly over predicts the stress relaxation and creep behavior under long-term exposure. The deviation between the predicted and experimental results after the initial stage was explained by examining the microstructure of G18 that shows the ceramic crystallites embedded into a matrix of a glassy phase [15]. The time-dependent behavior of the G18 composite is due to the viscous flow of the glassy phase. Since the crystallites behave elastically, the stress redistribution occurring inside the composite renders the relaxation longer than in a purely isotropic visco-elastic body.

In order to capture the longer term creep behaviors under different temperatures, the Maxwell-based damage model was further improved by introducing a separate ceramic crystalline phase, i.e., a standard visco-elastic solid model [14] with damage. The rate and temperature-dependent constitutive relationship for G18 can be expressed with the individual phase properties as [14]:

$$\dot{\varepsilon} + \frac{E_G(T)E_E}{\eta(E_G(T) + E_C)}\varepsilon = \frac{\dot{\sigma}}{E_G(T) + E_C} + \frac{E_G(T)\sigma}{\eta(E_G(T) + E_C)} \quad (5)$$

where ε represents strain, σ represents stress, η is the viscosity of the glassy phase, and E_G and E_C represent the Young's modulus of the glass and ceramic phase respectively. Using the temperature-dependent creep test data similar to those shown in Fig. 5, the material constants in Eq. (5) were quantified, and the corresponding constitutive model for G18 was implemented in the finite element-based stack creep analyses [16].

5.2. Implementation of glass seal interfacial properties

Given the interfacial strength properties measured in Tables 4 and 5, possible interfacial failure at the seal/interconnect interfaces can be predicted in an SOFC stack analyses by incorporating the critical strength in the selected failure criterion for the corresponding interface. For example, considering the combination of tensile and shear loading, a combined interfacial failure criterion has been proposed and implemented for the seal/interconnect interface:

$$\max\left(0, \frac{\sigma}{\sigma_{max}(T)}\right) + \left|\frac{\tau}{\tau_{max}(T)}\right| = 1 \quad (6)$$

in which $\sigma_{max}(T)$ and $\tau_{max}(T)$ are the temperature-dependent interfacial tensile and shear strength tabulated in Tables 4 and 5.

It should be mentioned that fracture mechanics-based failure criterion can also be implemented in the stack finite element analyses should the interfacial fracture toughness be available at different temperatures. A local finite element fracture mechanics analysis with specified size and location of pre-existing cracks will yield the stress intensity factors (SIF) at the interfacial crack tip, and the SIF can be compared with the interfacial fracture toughness to assess the interface integrity. Here, we chose the overall strength-based failure criterion due to its simplicity in experimental quantification and ease of implementation in finite element-based stack simulations.

6. Conclusions

This paper describes the measurement procedures and the typical results for glass–ceramic seal material properties and seal/interconnect interfacial properties for planar SOFC applications. We also presented the procedures in developing the corresponding constitutive relations for the glass–ceramic seal under different temperatures and loading conditions.

It is found that the glass–ceramic seal material properties strongly depend on the aging time and the corresponding crystalline phase volume fraction in the seal material. In addition, because of the existence of the residual glassy phase in the seal microstructure, the seal also shows considerable time and temperature-dependent long-term creep behaviors. The results and the modeling procedures presented in this paper will enable the accurate modeling of both short and long-term behavior of the SOFC system from the seal perspective. Taken collectively, these properties will allow accurate models that will serve to investigate long-term behavior of the stack and identify weak points in materials behavior or stack design with minimal cost and time.

Acknowledgements

This paper was funded as part of the Solid-State Energy Conversion Alliance (SECA) Core Technology program by the U.S. Department of Energy's National Energy Technology Laboratory. Pacific Northwest National Laboratory is operated by Battelle Memorial Institute for the U.S. Department of Energy under Contract No. DE-AC05-76RL01830.

References

[1] K.D. Meinhardt, J.D. Vienna, T.R. Armstrong, L.R. Pederson, "Glass-Ceramic Material and Method of Making," U.S. Patent 6,430,966 (2002).
[2] K.D. Meinhardt, J.D. Vienna, L.R. Pederson, T.R. Armstrong, "Glass-Ceramic Joint and Method of Joining," U.S. Patent 6,532,769 (2003).
[3] B.J. Koeppel, J.S. Vetrano, B.N. Nguyen, X. Sun, M.A. Khaleel, Proceedings of the 30th International Conference on Advanced Ceramics and Composites, Cocoa Beach, FL, 2006, Jan.
[4] K.S. Weil, J.E. Deibler, J.S. Hardy, D.S. Kim, G. Xia, L.A. Chick, C.A. Coyle, J Mater. Eng. Perf. 13 (3) (2004) 316–326.
[5] Z. Yang, G. Xia, K.D. Meinhardt, K.S. Weil, J.W. Stevenson, J Mater. Eng. Perf. 13 (3) (2004) 327–334.
[6] ASTM C1198-01, ASTM International, West Conshohocken, PA (2005).
[7] ASTM E228-95, ASTM International, West Conshohocken, PA (2005).
[8] ASTM C1161-02, ASTM International, West Conshohocken, PA (2005).
[9] ASTM C1211-02, ASTM International, West Conshohocken, PA (2005).
[10] ASTM D2095-96, ASTM International, West Conshohocken, PA (2005).
[11] ASTM F734-95, ASTM International, West Conshohocken, PA (2005).
[12] W.N. Liu, X. Sun, M.A. Khaleel, J. Power Sources 185 (2) (2008) 1193–2000.
[13] B.N. Nguyen, B.J. Koeppel, S. Ahzi, M.A. Khaleel, P. Singh, J. Am. Ceram. Soc. 89 (4) (2006) 1358–1368.
[14] Y.C. Fung, Biomechanics, 2nd ed., Springer-Verlag, New York, 1993, ISBN 0-387-97947-6.
[15] B.N. Nguyen, B.J. Koeppel, J.S. Vetrano, M.A. Khaleel, Proceedings of the 4th International Conference on Fuel Cell Science, Engineering, and Technology, Irvine, CA, 2006, June.
[16] N. Govindaraju, W.N. Liu, X. Sun, P. Singh, R.N. Singh, Parametric Modeling Study on the Behavior of Glass Ceramic and Self Healing Glass Seals for a Planar SOFC: Part I, Joint SECA topical report by University of Cincinnati and Pacific Northwest National Laboratory, 2007, PNNL-17529.